ACS APPLIED MATERIALS & INTERFACES
Research Article
www.acsami.org

Atomic Layer Deposition-Derived Ultra-Low-Density Composite Bulk Materials with Deterministic Density and Composition

Monika M. Biener,* Juergen Biener, Yinmin M. Wang, Swanee J. Shin, Ich C. Tran, Trevor M. Willey, Frédéric N. Pérez, Jon F. Poco, Stuart A. Gammon, Kevin B. Fournier, Anthony W. van Buuren, Joe H. Satcher, Jr., and Alex V. Hamza

Nanoscale Synthesis and Characterization Laboratory, Lawrence Livermore National Laboratory, 7000 East Avenue, Livermore, California 94550, United States

Supporting Information

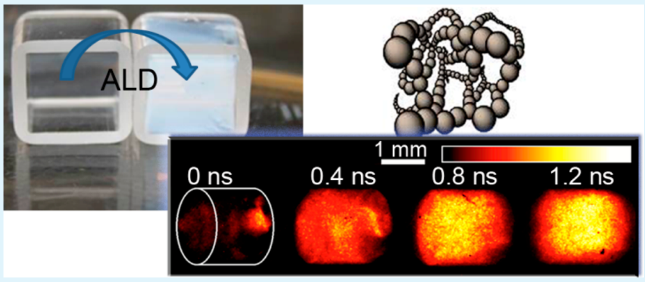

ABSTRACT: A universal approach for on-demand development of monolithic metal oxide composite bulk materials with air-like densities (<5 mg/cm^3) is reported. The materials are fabricated by atomic layer deposition of titania (TiO_2) or zinc oxide (ZnO) using the nanoscale architecture of 1 mg/cm^3 SiO_2 aerogels formed by self-organization as a blueprint. This approach provides deterministic control over density and composition without affecting the nanoscale architecture of the composite material that is otherwise very difficult to achieve. We found that these materials provide laser-to-X-ray conversion efficiencies of up to 5.3%, which is the highest conversion efficiency yet obtained from any foam-based target, thus opening the door to a new generation of highly efficient laser-induced nanosecond scale multi-keV X-ray sources.

KEYWORDS: *ultra-low-density foam, aerogels, atomic layer deposition, core−shell composite material, titanium dioxide, zinc oxide, lasers, X-ray source*

INTRODUCTION

Monolithic porous bulk materials with air-like densities have recently attracted renewed interest[1−5] because of many emerging applications in catalysis, energy storage and conversion, thermal insulation, shock energy absorption, and high-energy density physics.[6−11] The longest known low-density bulk materials are aerogels[12] whose self-similar, fractal network structure is formed by cross-linking colloidal nanoparticles,[13] but despite the tremendous progress that has been made since their discovery more than 80 years ago,[12,14] the realization of ultra-low-density aerogels with densities of <5 mg/cm^3 remains extremly challenging. The difficulty is that reducing the density often results in unpredictable changes in the morphology or even collapse of the structure as both the stiffness and strength of porous materials decrease at a more than linear rate as the density decreases, typically following a quadratic or stronger scaling relationship.[15] An exception is the especially robust SiO_2 sol−gel system that allows fabrication of high-quality bulk samples with densities that are lower than that of the air that fills their pores (1.2 mg/cm^3 at 760 Torr and 20 °C),[15] and although other recently developed synthesis approaches are capable of generating <5 mg/cm^3 bulk materials, they are either limited to carbon with graphene as the structural building block[1,2] or restricted to micrometer-sized features.[4]

Here, we report on rapid, on-demand development of monolithic, ultra-low-density (<5 mg/cm^3), mid-to-high-atomic number (Z) composite bulk materials with deterministic control over density and composition. Although our work is motivated by the needs of the Lawrence Livermore National Laboratory to develop brighter, nanosecond scale X-ray (∼5−10 keV) sources obtained by laser-irradiating high-Z materials, ultra-low-density monolithic porous bulk materials have many other promising applications. Laser-induced nanosecond X-ray sources can be used, for example, to obtain radiographs from imploding inertial fusion capsules. A promising approach to increasing the brightness of laser-created X-ray sources is to replace the traditional metallic foil targets by an ultra-low-density high-Z foam material.[10] The idea is to increase the laser-to-X-ray conversion efficiency by volumetric heating of the target material, which requires that the laser irradiation penetrates through the entire volume of a millimeter-sized target. This requirement limits the foam density to below ∼7 mg/cm^3 because below this density a laser heating wave propagates supersonically through the material,[16] forming a plasma without hydrodynamic motion of the target material and thus producing a flat density profile with negligible density

Received: September 24, 2013
Accepted: November 27, 2013
Published: November 27, 2013

gradients and flow velocities. Above this density, the laser deposits its energy locally over a small spatial scale and the energy goes into bulk hydrodynamic motion of the ablated material rather than heating the target material. Further, in the ablated material, laser light is scattered by laser-driven instabilities[17] (Raman scattering, Brillouin scattering, and filamentation) and is unavailable to then heat the target. Other requirements are that the solid should ideally be uniformly distributed on the length scale of the laser light, thus eliminating engineered microlattices[4] as possible templates, and that the high-*Z* atomic fraction should be as high as possible to achieve high conversion efficiencies, which eliminates the use of higher-density templates. The uniformity of laser heating is important as it creates a homogeneous X-ray source that provides higher-quality radiographs than an X-ray backlighter with gradients in either the source strength (i.e., surface brightness) or the spectral content.[18,19]

Here, we use recently developed high-quality 1 mg/cm^3 SiO_2 aerogel bulk samples[15] as robust nanoscale scaffolds that can be homogeneously coated to the desired density and composition using atomic layer deposition (ALD). As previously demonstrated, ALD is ideally suited to uniformly coat ultra-high-aspect ratio materials with atomic scale thickness control,[20−24] thus providing the desired deterministic control over density and composition. The atomic scale control over film thickness provided by ALD is the result of using a suitable pair of sequential, self-limiting surface reactions to deposit a desired material.[25] The concept of fabricating monolithic metal oxide composite bulk materials with air-like densities by ALD coating of 1 mg/cm^3 SiO_2 aerogel bulk samples was tested for TiO_2 and ZnO but can be easily extended to other ALD processes or combinations thereof that use sufficiently volatile precursor species. We find that our approach results in doping (Ti) concentrations much higher than those of previous attempts to fabricate TiO_2-doped silica aerogels by copolymerization of fixed ratios of tetramethoxysilane (TMOS) and titanium(IV) ethoxide monomers.[26]

■ RESULTS AND DISCUSSION

Optical images from 1 mg/cm^3 SiO_2 aerogels before and after being coated with TiO_2 and ZnO ALD are shown in Figure 1 and Figure 1 of the Supporting Information, respectively. While the uncoated SiO_2 aerogels are practically invisible under white light illumination, the material turns increasingly opaque with an increasing number of ALD cycles (Figure 1 of the Supporting Information). The material seems to be homogeneously coated as revealed by optical inspection.

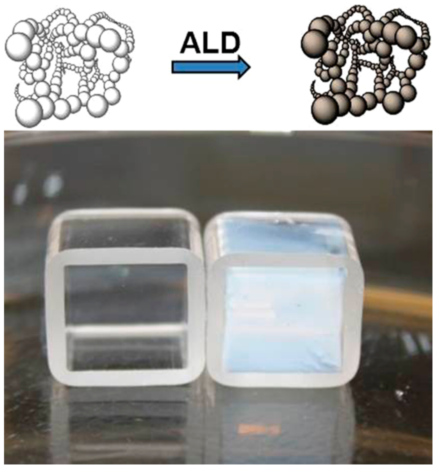

Figure 1. Optical image of 1 mg/cm^3 SiO_2 aerogels before (left) and after (right) being coated with 30 cycles of TiO_2 ALD. The uncoated SiO_2 aerogel is practically invisible but turns increasingly opaque with an increasing number of ALD cycles.

Both composition and uniformity were studied by Rutherford backscattering spectrometry (RBS), and representative data obtained from metal oxide-coated SiO_2 scaffold materials (MO−SiO_2) are shown in Figure 2a together with depth profiles of the atomic fractions of Ti and Zn (Figure 2b). RUMP code simulations (Figure 2a,b, solid lines) confirm that the material homogeneously coated the RBS detection depth (500 *μ*m). For the example shown in Figure 2a, the atomic fractions of Ti (30 cycles) and Zn (eight cycles) are ∼19 and 23%, respectively, and do not change with depth. The atomic

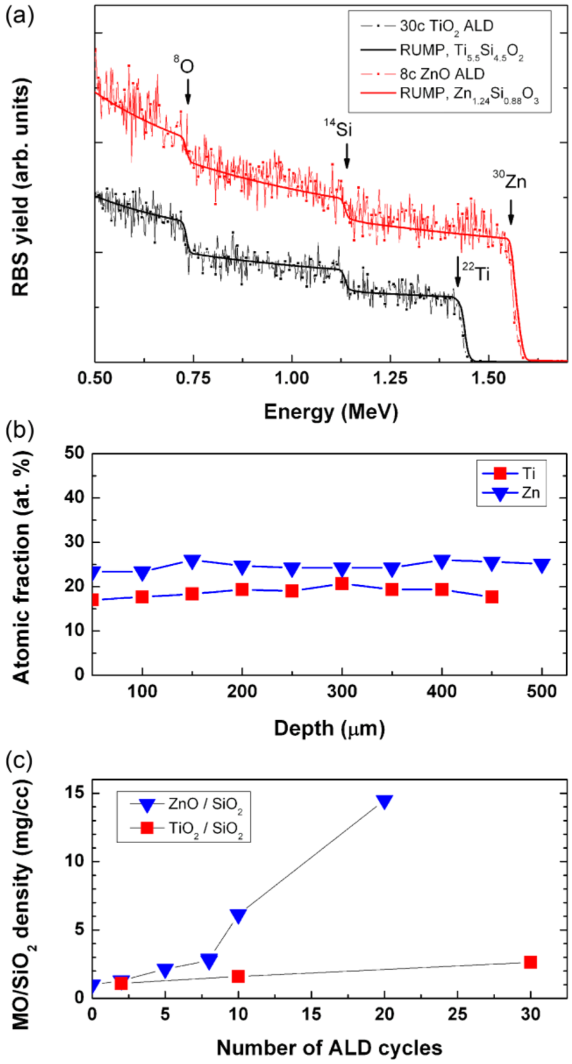

Figure 2. Composition and depth uniformity of ALD-coated SiO_2 scaffolds. (a) RBS spectra of TiO_2-coated (30 cycles) and ZnO-coated (eight cycles) 1 mg/cm^3 SiO_2 scaffolds. The positions of the surface peaks of O, Si, Ti, and Zn are denoted. Solid lines are the result of RUMP simulations. (b) Depth profiles of the Ti and Zn concentrations extracted from these RBS spectra. (c) Density vs number of ALD cycles for both TiO_2- and ZnO-coated SiO_2 scaffolds calculated form RBS composition data.

composition provided by RUMP code simulations was also used to calculate the density of the MO−SiO_2 composite materials (Figure 2c). For TiO_2, the density of the composite material increases approximately linearly with the number of ALD cycles at a rate of ~0.05 mg/cm^3 per TiO_2 ALD cycle (Figure 2c). For ZnO, the density increases up to 20-fold faster (up to ~1 mg/cm^3 per cycle). The high growth rate observed for the ZnO ALD process on the SiO_2 scaffold suggests a non-ideal ALD behavior as the growth rates for TiO_2 and ZnO reported in the literature differ by a factor of only ~2.5 (0.19 nm for ZnO[27] vs 0.078 nm for TiO_2[28]). Note, however, that the non-ideal behavior of the ZnO ALD process does not affect the compositional uniformity of the ZnO−SiO_2 composite material (Figure 2b). The ZnO ALD process also seems to have a nucleation-related induction period as the density increases at a 4-fold slower rate during the first eight cycles (~0.25 mg per cycle, which is still 5 times the TiO_2 ALD growth rate). Very similar results were obtained by weight measurements, although with larger error bars because of the extremely small sample mass (1−5 mg).

The nanoscale morphology of the SiO_2 scaffold as well as of the coated composite materials is illustrated by the transmission electron microscopy (TEM) images shown in Figure 3 and Figure 2 of the Supporting Information, respectively. The SiO_2 aerogel (Figure 3a) and the coated materials (Figure 3b,c) have very similar nanoscale morphologies that consist of ~10 nm wide ligaments. The deposited TiO_2 is not readily distinguishable from the underlying SiO_2 scaffold because both the SiO_2 ligaments and the deposited TiO_2[29] are amorphous, and their atomic numbers are similar, thus providing little contrast. Nevertheless, the fact that the formation of larger TiO_2 particles is not observed implies that the coating is conformal and uniform. The uniformity of the TiO_2 coating is further substantiated by selected-area TEM−EDX analysis as the Ti/Si ratio was found to be nearly independent of the size of the analyzed area. By contrast, individual crystalline ZnO nanoparticles seem to decorate the ZnO-coated SiO_2 scaffold (Figure 3c,d). The observation of individual crystalline ZnO nanoparticles [can be indexed to wurtzite phase (see the inset selected area diffraction pattern of Figure 3d)] is consistent with the idea of a low nucleation density suggested by the observation of an induction period (Figure 2b).

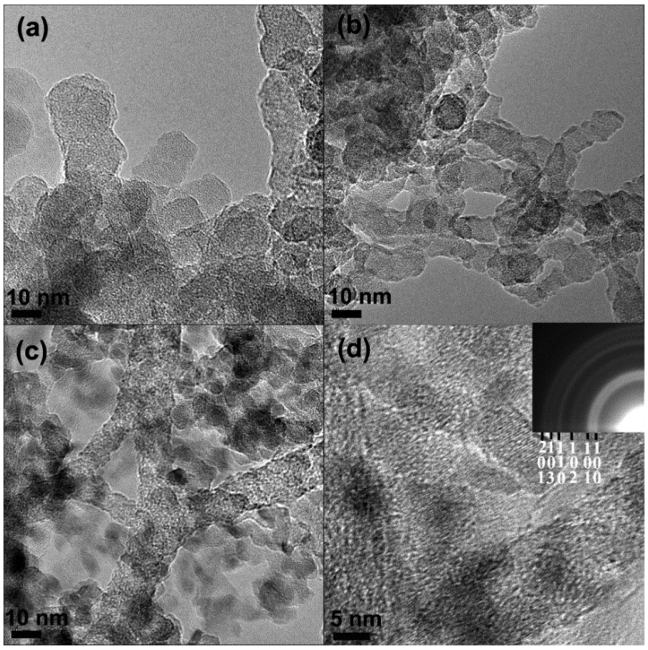

Figure 3. Morphological characterization of MO−SiO_2 aerogel composite materials. Bright-field TEM images of the SiO_2 scaffold before (a) and after deposition of 10 cycles of TiO_2 (b) or eight cycles of ZnO (c and d). Both the SiO_2 scaffold and the TiO_2 coating are amorphous, whereas the ZnO ALD particles are crystalline as revealed by both high-resolution TEM and the selected area diffraction pattern shown in panel d.

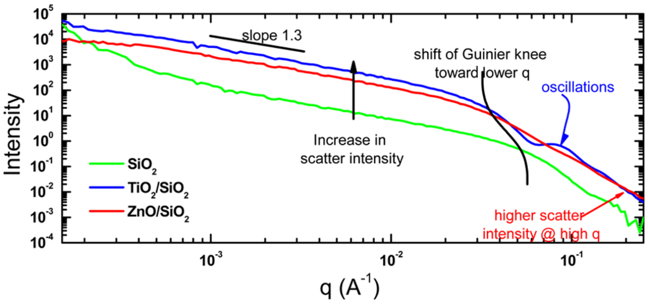

Figure 4. Characterization of the nanoscale morphology of uncoated and metal oxide-coated SiO_2 aerogels by USAXS. Background-corrected and slit-desmeared USAXS profiles of the uncoated and TiO_2- or ZnO-coated SiO_2 composite materials.

The nanoscale morphology of the MO−SiO_2 composite materials was further studied nondistructively by ultra-small-angle X-ray scattering (USAXS), and a typical set of background-corrected and desmeared USAXS spectra is shown in Figure 4. Two district regimes with different scattering responses are observed for both uncoated and MO-coated SiO_2 aerogels: (1) the curved Guinier high-*q* region above 10^{-2} Å^{-1} that represents scattering from the primary MO−SiO_2 nanoparticles and (2) the relatively flat low-*q* region (<10^{-2} Å^{-1}) with a power law slope close to 1 that suggests more or less linear ligament aggregates (mass fractal dimension). Note that the slope does not change upon ALD coating, thus indicating that ALD does not change the ligament morphology on the mass fractal length scale. However, several ALD-related effects can be observed. (1) The overall scattering intensity increases because of the added scattering contrast from the metal oxide ALD coatings (the X-ray scattering contrasts for SiO_2, TiO_2, and ZnO are 503, 1166, and 1973 × 10^{20} cm^{-4}, respectively). Note that the absolute scattering intensity of eight-cycle ZnO−SiO_2 sample is smaller than that of the 30-cycle TiO_2−SiO_2 sample, although both coating conditions lead to similar density increases, from ~1 mg/cm^3 for the uncoated SiO_2 aerogel to ~3 mg/cm^3 (Figure 2b). The lower intensity of eight-cycle ZnO is a consequence of the ~50% higher density of ZnO (5.6 g/cm^3 vs ~3.8 g/cm^3 for amorphous TiO_2[30]) and thus thinner coating. (2) The main Guinier knee shifts toward a lower *q*, from ~0.052 to 0.035 Å^{-1}, consistent with an overall size increase of the SiO_2 ligaments due to ALD coating. (3) The oscillations[31] observed in the high-*q* region of the TiO_2−SiO_2 scattering signal underline the uniformity of the TiO_2 coatings demonstrated by TEM (Figure 3b). (4) The scattered intensity of the ZnO−SiO_2 sample at high *q* values (>0.2 Å^{-1}) is higher than that from the TiO_2−SiO_2 sample, although the latter starts with a higher intensity at lower *q* values. The additional intensity of the ZnO−SiO_2 sample at high *q* values can be attributed to scattering from the crystalline ZnO nanoparticles, as detected by TEM (Figure 3c). In an attempt to extract more detailed structural information, the experimental USAXS profiles of the MO−SiO_2 samples were least-squares fit using a core−shell scattering model. Details regarding the fitting procedure can be found in the Supporting Information.

In short, the analysis confirms the overall network morphology observed by TEM as both uncoated and metal oxide-coated SiO_2 particles have USAXS-derived particle diameters of ∼8−9 nm (Figure 3 of the Supporting Information). The coating thickness derived by USAXS is ∼2.8 and 0.26 nm for TiO_2 (30 cycles) and ZnO ALD (eight cycles), respectively. In the case of TiO_2, the USAXS-derived coating thickness is in excellent agreement with the expected layer thickness of a 30-cycle TiO_2 ALD coating (30 × 0.078 nm/cycle = 2.34 nm). The USAXS-derived ZnO coating thickness, however, is much lower than expected from the RBS-derived mass gain, thus demonstrating that the core−shell model is not suitable for describing the morphology of the ZnO−SiO_2 material as expected from the observation of crystalline ZnO nanoparticles in TEM micrographs (Figure 3d). The analysis also reveals that both the uncoated SiO_2 and the TiO_2-coated SiO_2 aerogels have narrow size distributions centered around 8−9 nm (Figure 3 of the Supporting Information).

Finally, we tested the performance of the MO−SiO_2 composite materials as multi-keV X-ray sources at the Omega laser facility[32] (Laboratory for Laser Energetics, University of Rochester, Rochester, NY). All targets were irradiated by 40 laser beams for a total of 20 kJ on target at a wavelength of 351 nm.[26] The experiments revealed that the MO−SiO_2 composite materials discussed above have very high laser-to-X-ray conversion efficiencies (CEs). A photograph of such a low-density TiO_2−SiO_2 composite foam target (2 mg/cm^3 TiO_2 and 1 mg/cm^3 SiO_2, ∼20 atom % Ti) is presented in Figure 5a, and a schematic of the laser beam configuration is shown in Figure 5b. Snapshot images of ∼4.7 keV X-ray emission at different times during laser irradiation, displayed in Figure 5c, show uniform emission throughout the whole volume, indicating penetration of the laser through the whole foam material. Absolute measurements of the X-ray output reveal that TiO_2−SiO_2 composite foam targets with 20 atom % Ti have a laser-to-X-ray CE of 5.3% in an energy band from 4.5 to 6.0 keV. This appears much higher than the CE values measured on lower-Ti concentration foam targets (CE of 0.8% for 4 atom % Ti) during the same experiment and exceeds the performance of thick-foil targets (CE of 3%).[33,34] This is actually the highest CE yet obtained from any foam-based target. High-concentration Zn foams were also tested in the same configuration. They showed a CE of 1% in the band from 9 to 11 keV, which is the highest yet reported from a Zn material. Overall, the high CE of the MO−SiO_2 composite foam targets described here will open the door to new applications of laser-induced X-ray generation. The possibility to easily adjust composition and density greatly facilitates the optimization of these targets.

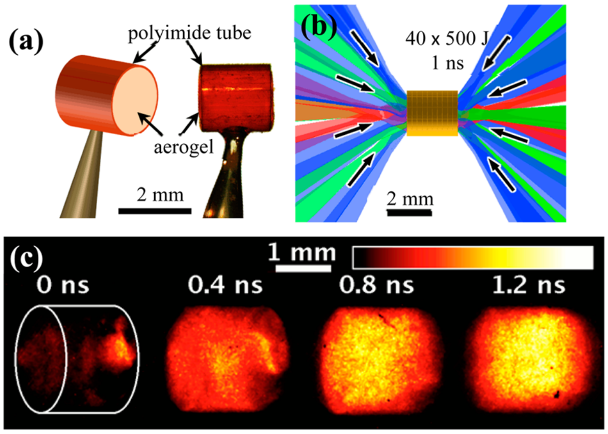

Figure 5. Multi-kiloelectronvolt laser-induced X-ray sources for radiography. (a) Schematics and photograph of a cylindrical low-density foam target. (b) Schematic of the laser beam configuration of the Omega laser for X-ray source experiments. (c) Snapshots of ∼4.7 keV X-ray emission from a 2 mg/cm^3 TiO_2−1 mg/cm^3 SiO_2 composite target at different times during the laser irradiation demonstrating volumetric X-ray generation.

CONCLUSIONS

The ALD-based approach described here provides a path toward the development of ultra-low-density foam materials with deterministic control over density and composition. Compared to traditional sol−gel-based foam development, the ALD approach described here not only drastically reduced the developing time but also provided better performing materials for the laser-induced X-ray source application. The ALD approach is universal and can easily be expanded to even more complex ternary or quaternary materials by combining different ALD processes. We expect this to have far-reaching implications in the fields of catalysis and sensor applications. Beyond the synthesis of new functional materials, ALD also provides an opportunity to further characterize ultra-low-density materials that are often very difficult to assess by traditional characterization methods because of the lack of contrast or mechanical instability. For example, the ALD-induced mass gain can also be used to calculate the specific surface area of ultra-low-density foam materials that otherwise cannot be assessed by BET measurements because of deformation or collapse of the structure during wetting with cryogenic N_2. For the 1 mg/cm^3 SiO_2 aerogels used in this study, the observed mass gain of ∼0.05 mg/cm^3 per TiO_2 ALD cycle translates into a calculated surface area of ∼200 m^2/g (assuming a growth rate of 0.078 nm TiO_2 per cycle[28]). This is close to the surface area of 207 m^2/g of a hypothetical material that consists of 13 nm diameter spherical particles of amorphous SiO_2 (density of ∼2.2 g/cm), thus validating the approach to estimating the surface area of ultra-low-density materials from the experimentally observed ALD-induced weight gain.

EXPERIMENTAL SECTION

Synthesis of Materials. SiO_2 aerogels with a density of ∼1 mg/cm^3 were prepared as described previously[15] using a two-step sol−gel chemistry approach and the high-temperature fast-reactor solvent extraction method developed by Poco and co-workers.[35] The details of aerogel synthesis can be found in ref 15. The aerogels were cast in either cubic glass molds (volume of 1 cm^3) or, for laser experiments, in 2 mm diameter polyimide tubes ($C_{22}H_{10}N_2O_5$, 50 μm wall thickness and 2 mm length). The uncoated aerogels were monolithic and practically invisible under white light illumination. The target density of the uncoated SiO_2 aerogels (1 mg/cm^3) was confirmed by measuring the mass of samples that were cast in 1 cm^3 molds. The SiO_2 aerogel was then converted to a material with the desired composition and density (for this application, <5 mg/cm^3) by being coated with 2–30 cycles of either a titanium tetrachloride ($TiCl_4/H_2O$)[28] or diethyl zinc ($ZnEt_2/H_2O$) ALD process[23] using a warm wall reactor (wall and stage temperature of 110 °C). To facilitate handling, the aerogels were kept in their molds during coating. Long pump (20 s), pulse (500 s at ~133 Pa), and nitrogen purge cycles (500 s) were used to ensure uniform coatings throughout the porous material.

Characterization of Materials. The composition and depth uniformity were measured by Rutherford backscattering spectrometry (RBS, 2.0 MeV $^4He^+$ ions, scattering angle of 164°) and RUMP code simulations.[36] Multiple scattering events are not expected to affect the results of our RUMP code simulations because their contribution is so small in absolute value, especially at the higher-energy side where we determine the composition. The mass gain of the coated samples was calculated from the composition determined by RBS as direct weight measurements resulted in larger error bars. The nanoscale morphology of the ligaments of the aerogel was characterized by bright field transmission electron microscopy (BF-TEM), and the overall morphology of the material (size, shape, and distribution of the structural elements) was assessed by USAXS using the Bonse-Hart double-crystal USAXS instrument on beamline 15ID-D at the Advanced Photon Source (Argonne National Laboratory, Argonne, IL).[37,38] For each sample, slit-smeared one-dimensional data were collected in transmission mode by using a photon beam energy of 17.0 kV (λ = 0.72932 Å), covering a scattering angular range (**q** vector) from 10^{-4} to 0.3 $Å^{-1}$. The raw data were corrected for background using the small-angle scattering profile of air as a reference sample. Irena and Indra[31] (available online at http://usaxs.xor.aps.anl.gov) were employed to correct and desmear the USAXS data. The slit-desmeared data for uncoated SiO_2 aerogels were then least-squares fit using log-normal distributions of scatterers, having a form factor of spheroids. For TiO_2- and ZnO-coated SiO_2 aerogels, a core–shell model of scatterers was used.

Laser-Induced Nanosecond Scale Multi-Kiloelectronvolt X-ray Generation. The performance of the MO–SiO_2 composite materials as multi-kiloelectronvolt X-ray sources was tested at the Omega laser facility[32] (Laboratory for Laser Energetics, University of Rochester). All targets were irradiated by 40 laser beams for a total of 20 kJ on target at a wavelength of 351 nm.

■ ASSOCIATED CONTENT

Ⓢ Supporting Information

Additional information about the characterization of materials. This material is available free of charge via the Internet at http://pubs.acs.org.

■ AUTHOR INFORMATION

Corresponding Author

*E-mail: biener3@llnl.gov.

Notes

The authors declare no competing financial interest.

■ ACKNOWLEDGMENTS

Work at Lawrence Livermore National Laboratory (LLNL) was performed under the auspices of the U.S. Department of Energy by LLNL under Contract DE-AC52-07NA27344. Project 13-LWD-031 was funded by the LDRD Program at LLNL. ChemMatCARS is supported by NSF and DOE under grant NSF/CHE-0822838. APS is supported by the DOE BES, under contract DE-AC02-06CH11357.

■ REFERENCES

(1) Mecklenburg, M.; Schuchardt, A.; Mishra, Y. K.; Kaps, S.; Adelung, R.; Lotnyk, A.; Kienle, L.; Schulte, K. *Adv. Mater.* **2012**, *24*, 3486–3490.

(2) Qiu, L.; Liu, J. Z.; Chang, S. L. Y.; Wu, Y.; Li, D. *Nat. Commun.* **2012**, *3*, 1241.

(3) Zhao, Y.; Hu, C. G.; Hu, Y.; Cheng, H. H.; Shi, G. Q.; Qu, L. T. *Angew. Chem., Int. Ed.* **2012**, *51*, 11371–11375.

(4) Schaedler, T. A.; Jacobsen, A. J.; Torrents, A.; Sorensen, A. E.; Lian, J.; Greer, J. R.; Valdevit, L.; Carter, W. B. *Science* **2011**, *334*, 962–965.

(5) Biener, J.; Stadermann, M.; Suss, M.; Worsley, M. A.; Biener, M. M.; Rose, K. A.; Baumann, T. F. *Energy Environ. Sci.* **2011**, *4*, 656–667.

(6) Gesser, H. D.; Goswami, P. C. *Chem. Rev.* **1989**, *89*, 765–788.

(7) Gibson, L. J.; Ashby, M. F. *Cellular solids: Structure and properties*, 2nd ed.; Cambridge University Press: Cambridge, U.K., 1997.

(8) Fournier, K. B.; Constantin, C.; Poco, J.; Miller, M. C.; Back, C. A.; Suter, L. J.; Satcher, J.; Davis, J.; Grun, J. *Phys. Rev. Lett.* **2004**, *92*, 165005.

(9) Fournier, K. B.; Satcher, J. H.; May, M. J.; Poco, J. F.; Sorce, C. M.; Colvin, J. D.; Hansen, S. B.; MacLaren, S. A.; Moon, S. J.; Davis, J. F.; Girard, F.; Villette, B.; Primout, M.; Babonneau, D.; Coverdale, C. A.; Beutler, D. E. *Phys. Plasmas* **2009**, *16*, 052703.

(10) Perez, F.; Kay, J. J.; Patterson, J. R.; Kane, J.; Villette, B.; Girard, F.; Reverdin, C.; May, M.; Emig, J.; Sorce, C.; Colvin, J.; Gammon, S.; Jaquez, J.; Satcher, J. H.; Fournier, K. B. *Phys. Plasmas* **2012**, *19*, 083101.

(11) Kucheyev, S. O.; Hamza, A. V. *J. Appl. Phys.* **2010**, 108.

(12) Kistler, S. S. *Nature* **1931**, *127*, 741–741.

(13) Vacher, R.; Woignier, T.; Pelous, J.; Courtens, E. *Phys. Rev. B* **1988**, *37*, 6500.

(14) Huesing, N.; Schubert, U. *Angew. Chem., Int. Ed.* **1998**, *37*, 23–45.

(15) Kucheyev, S. O.; Stadermann, M.; Shin, S. J.; Satcher, J. H.; Gammon, S. A.; Letts, S. A.; van Buuren, T.; Hamza, A. V. *Adv. Mater.* **2012**, *24*, 776–780.

(16) Denavit, J.; Phillion, D. W. *Phys. Plasmas* **1994**, *1*, 1971–1984.

(17) Kruer, W. L. *The Physics of Laser Plasma Interactions*; Westview Press: Boulder, CO, 2003.

(18) Landen, O. L.; Farley, D. R.; Glendinning, S. G.; Logory, L. M.; Bell, P. M.; Koch, J. A.; Lee, F. D.; Bradley, D. K.; Kalantar, D. H.; Back, C. A.; Turner, R. E. *Rev. Sci. Instrum.* **2001**, *72*, 627–634.

(19) Workman, J.; Fincke, J. R.; Keiter, P.; Kyrala, G. A.; Pierce, T.; Sublett, S.; Knauer, J. P.; Robey, H.; Blue, B.; Glendinning, S. G.; Landen, O. L. *Rev. Sci. Instrum.* **2004**, *75*, 3915–3920.

(20) Baumann, T. F.; Biener, J.; Wang, Y. M. M.; Kucheyev, S. O.; Nelson, E. J.; Satcher, J. H.; Elam, J. W.; Pellin, M. J.; Hamza, A. V. *Chem. Mater.* **2006**, *18*, 6106–6108.

(21) Biener, J.; Baumann, T. F.; Wang, Y. M.; Nelson, E. J.; Kucheyev, S. O.; Hamza, A. V.; Kemell, M.; Ritala, M.; Leskela, M. *Nanotechnology* **2007**, *18*, 055303.

(22) George, S. M. *Chem. Rev.* **2010**, *110*, 111–131.

(23) Kucheyev, S. O.; Biener, J.; Wang, Y. M.; Baumann, T. F.; Wu, K. J.; van Buuren, T.; Hamza, A. V.; Satcher, J. H.; Elam, J. W.; Pellin, M. J. *Appl. Phys. Lett.* **2005**, *86*, 083108.

(24) Elam, J. W.; Xiong, G.; Han, C. Y.; Wang, H. H.; Birrell, J. P.; Welp, U.; Hryn, J. N.; Pellin, M. J.; Baumann, T. F.; Poco, J. F.; Satcher, J. H. *J. Nanomater.* **2006**, *2006*, 64501.

(25) Leskelä, M.; Ritala, M. *Angew. Chem., Int. Ed.* **2003**, *42*, 5548–5554.

(26) Pérez, F.; Patterson, J. R.; May, M.; Colvin, J. D.; Biener, M. M.; Wittstock, A.; Kucheyev, S. O.; Charnvanichborikarn, S.; Satcher, J. H.; Gammon, S. A.; Poco, J. F.; Fujioka, S.; Zhang, Z.; Ishihara, K.; Tanaka, N.; Ikenouchi, T.; Nishimura; Fournier, K. B. *Phys. Plasmas* **2014**, to be submitted for publication.

(27) Keun Kim, S.; Seong Hwang, C.; Ko Park, S.-H.; Jin Yun, S. *Thin Solid Films* **2005**, *478*, 103–108.

(28) Aarik, J.; Aidla, A.; Mändar, H.; Uustare, T. *Appl. Surf. Sci.* **2001**, *172*, 148–158.

(29) Biener, M. M.; Biener, J.; Wichmann, A.; Wittstock, A.; Baumann, T. F.; Baeumer, M.; Hamza, A. V. *Nano Lett.* **2011**, *11*, 3085–3090.

(30) Hoang, V. V. *Nanotechnology* **2008**, *19*, 105706.

(31) Ilavsky, J.; Jemian, P. R. *J. Appl. Crystallogr.* **2009**, *42*, 347–353.

(32) Boehly, T. R.; Brown, D. L.; Craxton, R. S.; Keck, R. L.; Knauer, J. P.; Kelly, J. H.; Kessler, T. J.; Kumpan, S. A.; Loucks, S. J.; Letzring, S. A.; Marshall, F. J.; McCrory, R. L.; Morse, S. F. B.; Seka, W.; Soures, J. M.; Verdon, C. P. *Opt. Commun.* **1997**, *133*, 495−506.

(33) Girard, F.; Primout, M.; Villette, B.; Stemmler, P.; Jacquet, L.; Babonneau, D.; Fournier, K. B. *Phys. Plasmas* **2009**, *16*, 052704.

(34) Girard, F.; Primout, M.; Villette, B.; Stemmler, P.; Jacquet, L.; Babonneau, D.; Fournier, K. B. *Phys. Plasmas* **2011**, *18*, 079901.

(35) Poco, J. F.; Coronado, P. R.; Pekala, R. W.; Hrubesh, L. W. *Mater. Res. Soc. Symp. Proc.* **1996**, *431*, 297−302.

(36) Doolittle, L. R. *Nucl. Instrum. Methods Phys. Res., Sect. B* **1985**, *9*, 344−351.

(37) Ilavsky, J.; Jemian, P. R.; Allen, A. J.; Zhang, F.; Levine, L. E.; Long, G. G. *J. Appl. Crystallogr.* **2009**, *42*, 469−479.

(38) Ilavsky, J.; Zhang, F.; Allen, A. J.; Levine, L. E.; Jemian, P. R.; Long, G. G. *Metall. Mater. Trans. A* **2013**, *44A*, 68−76.